PHYSICAL REVIEW D VOLUME 12, NUMBER 9 1 NOVEMBER 1975

Backward $\pi^- p$ reactions between 0.6 and 1.0 GeV/c

N. C. Debenham, D. M. Binnie, L. Camilleri,* J. Carr, A. Duane, D. A. Garbutt, W. G. Jones, J. Keyne, and I. Siotis

Department of Physics, Imperial College, London, England

J. G. McEwen

Department of Physics, Southampton University, Southampton, England

(Received 16 June 1975)

Measurements are reported of the differential cross section for the reaction $\pi^- p \to \pi^- p$, $\pi^0 n$, and ηn at three angles close to 180° and for incident momenta in the range 0.6 to 1.0 GeV/c. The three measurements were made simultaneously at 1% intervals of beam momentum. The data on elastic scattering resolve a discrepancy between two earlier experiments. They also show clearly the effect of the opening of the ηn channel. The charge-exchange data show that I-spin bounds are not violated in the kinematic region covered. The ηn data can be adequately described with known s-channel resonances. No evidence for narrow N^*'s is seen in any channel.

I. EXPERIMENT

We present the results of an experiment performed at the Rutherford High Energy Laboratory to measure the differential cross sections of the reactions

$$\pi^- p \to p\pi^- ,$$

$$\pi^- p \to n\pi^0 ,$$

$$\pi^- p \to n\eta ,$$

at three angles close to 180° in the center-of-mass system, for pion momenta in the range 0.6–1.0 GeV/c. Figure 1 shows a plan of the apparatus, much of which was previously used for a study of meson thresholds.[1] A beam of negative pions was incident upon a liquid-hydrogen target 29.4 cm long, and the recoiling nucleons were detected in an array of ten "neutron" counters situated 7 m downstream of the target. A set of counters, A_{1-10}, covering the front faces of the neutron counters, determined the charge state of the nucleon. Reactions were further identified by a measurement of the recoil particle's time of flight, and by the detection of reaction products in an array of γ detectors and charged-particle detectors surrounding the hydrogen target. The direct detection of the nucleon enabled a precise determination of the scattering angle to be made and also allowed all three reactions to be observed simultaneously. This feature was combined with a fine resolution on the incident momentum with measurements at closely spaced intervals.

The beam of negative pions was produced by collisions of the circulating proton beam in Nimrod on an internal copper target, and was transported to the hydrogen target by a two-stage beam line. The first stage accepted a 3% bite of momenta and formed an image at an intermediate focus. The particles were momentum analyzed in the second stage and brought to a second focus in the hydrogen target. The spectrometer consisted of a bending magnet and quadrupole doublet with hodoscopes at conjugate foci of the doublet. With this system, beam particles were assigned to momentum bins of 1% separation; the momentum distribution in each bin being approximately triangular upon a base of width 2%. Three adjacent bins were accepted for each setting of the spectrometer central momentum.

Apart from some changes to the hodoscope counters, the techniques used were similar to those described in Ref. 2. Electrons in the beam were vetoed using a CO_2 gas Čerenkov counter, situated upstream of the spectrometer, and contamination by muons was measured in a separate experiment using a high-pressure Freon-13 gas Čerenkov counter. Typical numbers of useful beam particles accepted during the Nimrod spill time of about 200 msec were 3×10^4 at 0.6 GeV/c and 1.6×10^5 at 1.0 GeV/c.

The currents required in the spectrometer dipole and quadrupole magnets were determined by separate calibrations using the floating-wire technique. By tensioning the wire over an air-bearing pulley, the equivalent particle momentum could be determined to 0.02%[1,2]; and calibrations made before and after the data collection period agreed to within this accuracy. The momentum scale, which was determined by the dipole field, was transferred to the frequency scale of a nuclear-magnetic-resonance probe placed inside the magnet, by calibrating the spectrometer momentum at several settings and interpolating to intermediate

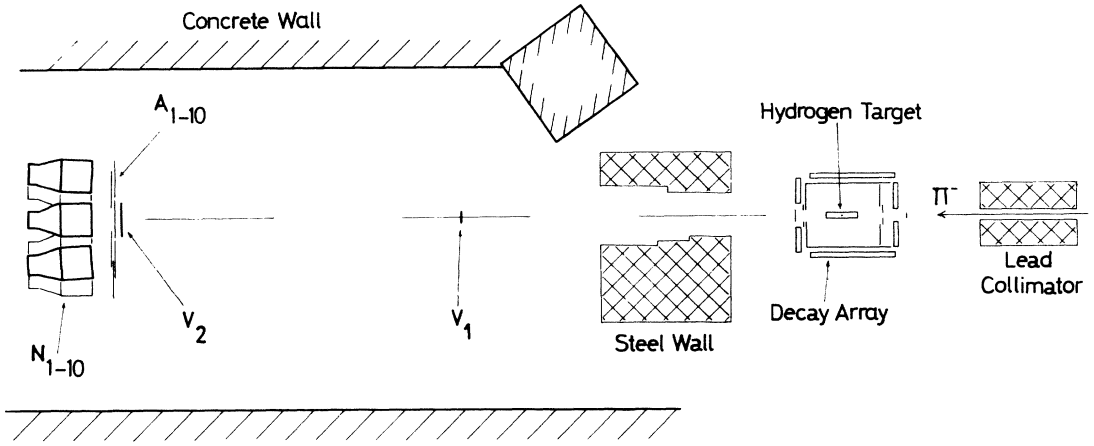

FIG. 1. Layout of apparatus. Negative pions enter from the right and either interact in the hydrogen target or are vetoed by counters V_1 and V_2. Neutrons and protons at angles up to 6.5° to the beam are detected in counters N_{1-10} and are distinguished by counters A_{1-10}. Details of the target region are shown in Fig. 2.

points. The dipole-magnet current was stable to 1 part in 10^4, and the currents in the quadrupole magnets to 1 part in 10^3.

The ten neutron counters each consisted of a cylindrical volume of NE 102A plastic scintillator, 30 cm in diameter by 30 cm deep, whose downstream circular face was viewed by a 58 AVP photomultiplier via a tapered light guide. The centers of their faces were arranged on three circles concentric to the beam axis. These circles lay in a plane 7 m downstream of the hydrogen target's center, where their radii subtended angles of 2.6°, 4.5°, and 6.5°, respectively. Four counters were arranged on the innermost ring, while the middle and outer rings contained three each. The time of flight was measured between a neutron counter and a beam counter S (Fig. 2). A full description of the operation of these counters can be found in Ref. 1. This reference also contains details of the on-line fast logic system.

The arrangement of the charge counters and γ detectors surrounding the hydrogen target is shown in Fig. 2. The counters P, R_1, and R_2, collectively referred to as the proton counter, intercepted all recoil particles that passed directly from the hydrogen target to the neutron counters, and could therefore be used to cross check the A counter firings. The rest of the decay array identified reaction products emerging from the target. The 47 γ detectors made up of 20 "lid" counters, LG, 19 "cylinder" counters, CG, and 8 "back" counters, BG, covered a 3.6π-sr solid angle about the target. They were faced by the charged-particle detectors, C_{1-20} and B_{1-3}. The array differs from that described in Ref. 1 in the addition of the back γ detectors. These counters used a three-layer lead-scintillator sandwich construction, with a total thickness of 4.2 radiation lengths, to convert and detect the γ's. They occupied eight of ten 36° azimuthal sectors about the beam axis and were designed to detect the high-energy (typically 200 MeV) γ's originating from the decay of neutral pions produced in the backward charge-exchange reactions, and did so with an efficiency of approximately 85%. The η's produced at backward angles in this experiment moved slowly in the laboratory system, and their decay products emerged almost isotropically from the hydrogen target. In particular, the opening angle between the γ's in the $\eta \to 2\gamma$ decay was close to 180°.

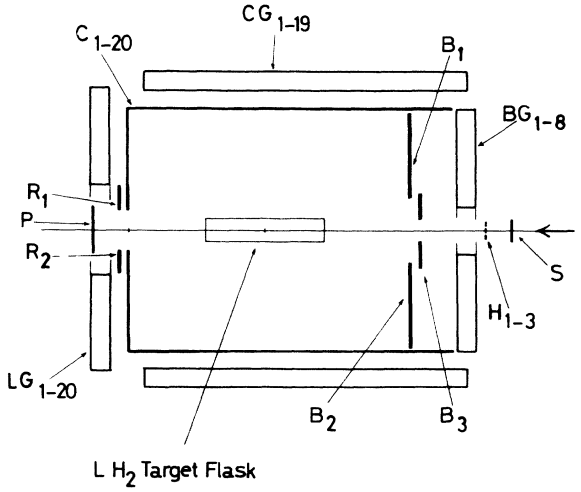

FIG. 2. Details of the decay array (Fig. 1). The hydrogen target is almost surrounded by charged-particle detectors P, R_{1-2}, C_{1-20}, and B_{1-3}, and γ counters LG_{1-20}, CG_{1-19}, and BG_{1-8}. Counter S defines the time of arrival of the π. Hodoscope counters H_{1-3} formed part of the π momentum spectrometer.

Backward elastically scattered pions were often detected in the back charge and γ counters, although approximately 40% of them escaped detection by passing out through the beam entrance hole. During the data collection period of 26 days, an average of 300-million incident pions was accumulated in each of the 52 1% momentum intervals between 0.6 and 1.0 GeV/c. Essentially all events with a delayed pulse from the neutron counters were recorded. In the subsequent analysis, the time-of-flight spectra were studied in conjunction with information available from the neutron counters and decay counters. The time of flight was determined with respect to the timing observed for fast scattered beam particles. A sample of such events, referred to as the "fast peak" was collected contemporarily with the data. The resolution of the spectra was maximized by applying corrections to the raw time-of-flight information for the neutron-counter pulse height (separately for neutrons and protons), and for the timing differences between individual counters.

II. DATA REDUCTION

The first aim of data reduction was to use the detailed information available for each event to reduce background levels. Residual backgrounds in the selected time-of-flight spectra were dominated by pion production processes, and their shapes were derived using Monte Carlo simulations of these reactions. The selection efficiencies, which were predicted to vary only slowly with momentum, were estimated from detailed studies of rejected events at selected momenta where the cross sections were large and the signal peaks well resolved. Efficiencies at other momenta were found by extrapolations based on Monte Carlo predictions.

A large class of triggers, at short time of flight, originated from the scattering of beam pions into the neutron counters from nearby structural material. Almost all of these events were eliminated by placing suitable requirements on the data. Most of the charged particles entering the neutron counters from the side were rejected by requiring that a single neutron counter had fired, and that the A-counter and proton-counter states agreed. Cuts in the neutron-counter pulse height were made to separate fast pions from the slower, more ionizing protons. The effect of these cuts can be seen in Fig. 3. The rejection of signal events in this process was measured to be (with some variations between the neutron-counter rings) approximately 12% for protons and 16% for neutrons. Reasons for the rejection of these events included cross talk between the neutron counters, and the

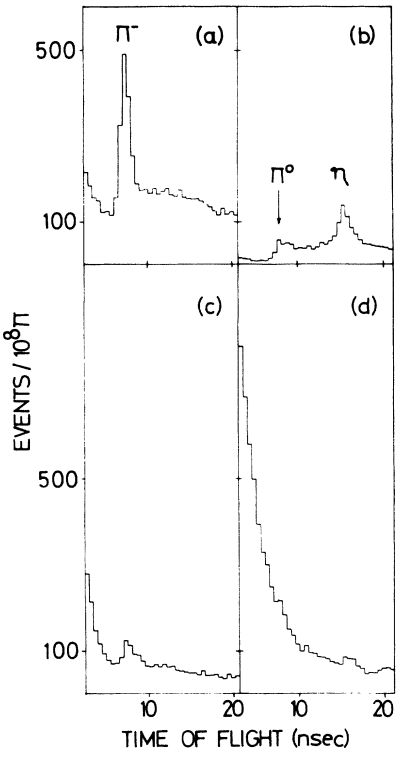

FIG. 3. Time-of-flight spectra for an incident momentum of 0.790 GeV/c. Selections of good proton (a) and neutron (b) events were made with suitable neutron counter and A counter requirements, and show signal peaks from elastic and charge-exchange scattering and η productions with backgrounds consisting mainly of pion production events. Rejected events, (c) and (d), are largely associated with fast beam pions which scatter near the neutron counters but include 12% of good proton and 16% of good neutron events.

failure of the pulse-height requirement by some of the neutron recoils. It was estimated that 2% of the η production events were rejected because they sent charged decay products into the proton counter.

From the remaining sample, elastic and charge-exchange scattering and η production events were selected by making suitable cuts using the decay array data. The cuts were designed to minimize the background levels under the peaks while preserving sizable proportions of the signal events. The η production sample was made up of 1γ events detected in the lid counters, 2γ events with large azimuthal separation of the γ's, and $>2\gamma$ events from the $\eta \to 3\pi^0$ decay. The charge-exchange scattering selection was composed of the remaining 1γ and 2γ events, and the elastic scattering sample required a charged particle to be detected in the back charged particle and γ detectors. Some typical time-of-flight spectra that resulted from

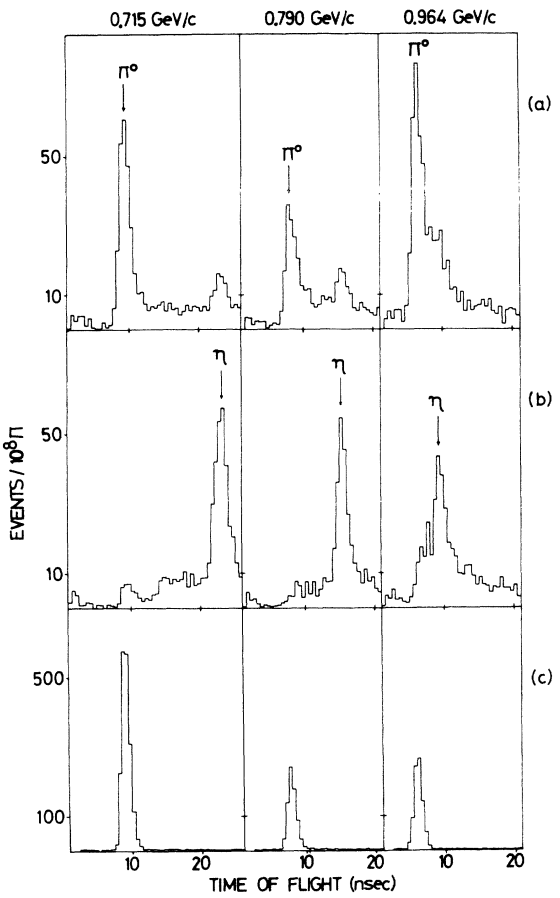

FIG. 4. Time-of-flight spectra, at three different momenta, in which reaction signals have been selected from the good neutron and good proton samples using the decay array information. The charge-exchange (a) and η production (b) selections show the effectiveness of the decay configuration cuts in separating the signals and the increasing proximity of the peaks with momentum. Backgrounds are contributed mainly by the $n\pi^0\pi^0$ final state. The elastic-scattering selections (c) were selected from the good proton sample by simply requiring a single charged particle in the back of the decay array.

these selections are shown in Fig. 4.

Backgrounds under the selected signal peaks were contributed mainly by the nonresonant one- and two-pion production reactions. Monte Carlo simulations were made of these reactions to study the shapes of their time-of-flight spectra. The interactions were randomly generated throughout the target volume, and, if the recoil nucleon entered the neutron counters, the interaction of the decay products with the counter array was simulated.[3] In this way, any effect of the decay selections on the background time-of-flight distributions was taken into account.

In the simulations which were carried out for twelve momenta over the range of the experiment, the reactions were first assumed to have phase-space mass distributions and isotropic productions in the c.m. system. The generated shapes were afterwards compared with samples of the background events (selected by suitable decay array cuts), and the mass and momentum-transfer distributions adjusted to give agreement. For the $p\pi^-\pi^0$ final state, the dipion mass distribution was found to be adequately predicted by phase-space considerations, but it was found necessary to weight the $n\pi^+n^-$ and $n\pi^0\pi^0$ dipion systems in favor of the higher masses. These finding are in agreement with previous observations.[4,5]

The shapes of the simulated time-of-flight spectra were extended to intermediate values of the incident momentum by fitting them and observing the variations of their fit parameters with energy. In the generation of the spectra, the errors in the experimental time-of-flight measurement, whether due to the depth of the neutron counters or present intrinsically in the electronics, were neglected. These effects were included later by convoluting the parametrized shapes with a Gaussian error function. The data required this function to have a standard deviation of 0.50 and 0.53 nsec for protons and neutrons, respectively.

Having derived the background shapes in this way, the time-of-flight spectra at every angle and momentum were fitted, and the numbers of events in the signal peaks measured. There were between 200 and 1200 signal events in each elastic-scattering spectrum. The charge-exchange selections contained between 150 and 800 signal events each, and the η production spectra around 200 events. The numbers were not sensitive to changes in background shapes. In the worst case, for charge-exchange signals at high momenta, a $\pm 5\%$ systematic error is ascribed to the measurements. As a further check on the subtraction of the backgrounds under the charge-exchange and η production peaks, measurements were made on a set of spectra in which the decay selections were made more restrictive and the background proportions correspondingly lower. For both reactions, the ratio between the amounts of signal in the different selections was constant with energy, as predicted by Monte Carlo calculations. Therefore, while the restricted selections suffered from a lack of statistics, and were not suitable for the final analysis, the measurements on them lent confidence to the background subtractions in the chosen selections.

The efficiencies with which the decay array cuts selected the reaction signals from the good recoil trigger samples were predicted from Monte Carlo studies to vary smoothly and slowly with momen-

tum, and it was therefore sufficient to determine them at a few momenta only. The measurements of the efficiencies were compared with the predictions of the Monte Carlo program. Agreement was good in the case of the η production signals, which has a selection efficiency of $(54 \pm 2)\%$, and the measurements are consistent with the known branching ratio for $(\eta \to \text{neutrals})/(\eta \to \text{total})$. Measurements of the elastic and charge-exchange scattering selection efficiencies became difficult for momenta above 0.75 GeV/c, where backgrounds under the total good recoil selections were high. Efficiencies in this region were determined by using the Monte Carlo predicted variations with energy to extrapolate the measured values from lower momenta. Selection efficiencies of the charge-exchange cuts, found in this way, were between 64% and 80% in the different neutron-counter rings, and varied with energy by not more than 4% in any given ring. The elastic-scattering selection was less efficient, between 48% and 64%, with up to 6% variation with momentum at any angle.

The efficiency of the neutron counters for detection of neutrons was calculated using the Monte Carlo program devised by Stanton.[6] This program is optimized to give agreement with measurements covering a variety of counter designs, neutron energies, and threshold biases. The kinetic energies of the neutrons observed in this experiment were all greater than 150 MeV, and in a region where the detection efficiency is approximately constant. The threshold for detected neutrons was measured to be 8 ± 2 MeV electron equivalent energy, but efficiencies were predicted to be not strongly dependent on this quantity. The calculated efficiency for normally incident neutrons, 0.240 ± 0.012, agrees well with an extrapolation from measurements made on these counters with up to 140-MeV neutron energy.[7]

The proportions of the measured signals which originated from interactions outside the liquid hydrogen were deduced from data collected at three momentum points with the target flask empty. This was done by remeasurement of the signal peaks after subtraction of the "hydrogen out" data, renormalized to the same number of incident pions. The necessary correction was small ($<4\%$) for η production events. For charge-exchange and elastic scattering, the corrections were larger and followed similar behaviors, rising from $(8 \pm 3)\%$ at 0.667 GeV/c to $(20 \pm 5)\%$ at 0.899 GeV/c. The correction, as a percentage, appeared to rise smoothly with momentum, and this was assumed to be the correct form in which to apply it. The assumption that it is the absolute number of events that varies smoothly with momentum leads to a lowering of the charge-exchange and elastic-scattering cross sections at their dips by 5% and by less elsewhere. The correction can be understood with a simple model in which the pions scatter on nucleons in a carbon nucleus.[8] This correctly predicts the increasing confusion of carbon and hydrogen scattering events with increasing energy.

In the calculation of the reaction cross sections, normalizations were corrected for a number of effects. Muon contamination amounted to 8% at 0.6 GeV/c, and 4.4% at 1.0 GeV/c. Other contaminants were negligible. The pion fluxes were corrected by 6% to allow for interaction losses before and within the hydrogen target. Monte Carlo calculations indicated that 2% of the elastic events detected in the innermost neutron-counter ring vetoed themselves by sending the scattered pion into the H counters. The loss of recoil particles by interactions in flight amounted to 4%, and 2% of the neutron recoils produced pulses in the A counters, whether by direct interaction or via the products of neutron-carbon reactions in the neutron counters. Neutrons which interacted in the A counters without triggering them caused a 1% increase in the effective length and efficiency of the neutron counters.

III. RESULTS

The differential cross sections for the elastic scattering and charge-exchange scattering are given in Table I, and those for the η production reaction in Table II. The quoted errors are the statistical uncertainties on the measurements. The values of the incident pion momenta are corrected for energy loss after the vacuum pipe, and carry an absolute error of $\pm 0.1\%$, due mainly to uncertainties in hodoscope positions relative to floating-wire points. The momentum distribution in each bin has a full width at half maximum FWHM of 1.2%. The solid angles subtended by the neutron counters in the c.m. system were calculated by a Monte Carlo method. For the scattering reactions, the inner, middle, and outer rings subtended ranges in $\cos\theta_{\text{c.m.}}$ with FWHM approximately equal to 0.006, 0.010, and 0.020, respectively.

Over-all normalization errors derive mainly from uncertainties in the selection efficiencies and nonhydrogen scattering subtractions. They vary, for the elastic-scattering cross sections, from $\pm 7\%$ at 0.6 GeV/c to $\pm 11\%$ at 1.0 GeV/c, and for charge-exchange scattering from $\pm 11\%$ to $\pm 14\%$ in the same momentum range. For η production, the uncertainty is $\pm 10\%$ throughout. These errors are largely uncorrelated over momentum intervals of more than about 15%, and, since selection efficiencies and background shapes vary appreciably

TABLE I. $\pi^- p$ elastic-scattering and charge-exchange differential cross sections.

P_π (GeV/c)	$\cos\theta_{c.m.}$	$\pi^- p \to \pi^- p$ $d\sigma/d\Omega$ (mb/sr)	$\pi^- p \to \pi^0 n$ $d\sigma/d\Omega$ (mb/sr)	P_π (GeV/c)	$\cos\theta_{c.m.}$	$\pi^- p \to \pi^- p$ $d\sigma/d\Omega$ (mb/sr)	$\pi^- p \to \pi^0 n$ $d\sigma/d\Omega$ (mb/sr)
0.5993	−0.995	1.273 ± 0.026	0.194 ± 0.018	0.7037	−0.995	1.370 ± 0.017	0.637 ± 0.022
	−0.986	1.242 ± 0.024	0.228 ± 0.021		−0.985	1.354 ± 0.017	0.660 ± 0.023
	−0.970	1.244 ± 0.026	0.248 ± 0.021		−0.969	1.384 ± 0.019	0.672 ± 0.023
0.6053	−0.995	1.287 ± 0.023	0.224 ± 0.017	0.7108	−0.995	1.271 ± 0.017	0.642 ± 0.022
	−0.986	1.259 ± 0.022	0.239 ± 0.019		−0.985	1.284 ± 0.017	0.645 ± 0.023
	−0.970	1.274 ± 0.023	0.226 ± 0.018		−0.969	1.319 ± 0.018	0.641 ± 0.023
0.6114	−0.995	1.342 ± 0.025	0.260 ± 0.020	0.7180	−0.995	1.178 ± 0.016	0.556 ± 0.020
	−0.986	1.254 ± 0.023	0.231 ± 0.020		−0.985	1.176 ± 0.015	0.631 ± 0.022
	−0.970	1.350 ± 0.026	0.263 ± 0.021		−0.968	1.213 ± 0.017	0.585 ± 0.021
0.6176	−0.995	1.280 ± 0.030	0.266 ± 0.025	0.7252	−0.995	1.066 ± 0.016	0.536 ± 0.021
	−0.986	1.326 ± 0.030	0.231 ± 0.024		−0.985	1.122 ± 0.016	0.557 ± 0.023
	−0.970	1.312 ± 0.032	0.265 ± 0.026		−0.968	1.161 ± 0.018	0.649 ± 0.024
0.6238	−0.995	1.341 ± 0.027	0.335 ± 0.025	0.7325	−0.995	1.026 ± 0.017	0.490 ± 0.021
	−0.986	1.319 ± 0.026	0.346 ± 0.027		−0.985	1.032 ± 0.016	0.589 ± 0.024
	−0.970	1.349 ± 0.029	0.322 ± 0.025		−0.968	1.046 ± 0.018	0.541 ± 0.023
0.6301	−0.995	1.401 ± 0.030	0.314 ± 0.026	0.7399	−0.995	0.889 ± 0.015	0.498 ± 0.020
	−0.986	1.327 ± 0.028	0.338 ± 0.028		−0.985	0.908 ± 0.015	0.544 ± 0.023
	−0.969	1.450 ± 0.032	0.292 ± 0.026		−0.968	0.936 ± 0.016	0.531 ± 0.022
0.6365	−0.995	1.331 ± 0.029	0.417 ± 0.030	0.7474	−0.995	0.826 ± 0.014	0.439 ± 0.019
	−0.986	1.357 ± 0.029	0.350 ± 0.029		−0.985	0.835 ± 0.014	0.478 ± 0.021
	−0.969	1.365 ± 0.031	0.371 ± 0.029		−0.968	0.879 ± 0.016	0.532 ± 0.022
0.6429	−0.995	1.322 ± 0.026	0.377 ± 0.025	0.7549	−0.995	0.704 ± 0.013	0.402 ± 0.019
	−0.986	1.374 ± 0.026	0.415 ± 0.028		−0.985	0.781 ± 0.014	0.478 ± 0.022
	−0.969	1.438 ± 0.029	0.392 ± 0.027		−0.968	0.778 ± 0.015	0.528 ± 0.023
0.6494	−0.995	1.428 ± 0.030	0.437 ± 0.030	0.7625	−0.995	0.617 ± 0.011	0.365 ± 0.016
	−0.986	1.401 ± 0.029	0.470 ± 0.033		−0.985	0.647 ± 0.012	0.420 ± 0.018
	−0.969	1.473 ± 0.032	0.435 ± 0.031		−0.968	0.693 ± 0.013	0.473 ± 0.019
0.6560	−0.995	1.409 ± 0.030	0.524 ± 0.034	0.7702	−0.995	0.553 ± 0.011	0.304 ± 0.014
	−0.986	1.418 ± 0.030	0.477 ± 0.034		−0.985	0.591 ± 0.011	0.431 ± 0.018
	−0.969	1.419 ± 0.032	0.382 ± 0.030		−0.968	0.629 ± 0.012	0.447 ± 0.018
0.6626	−0.995	1.430 ± 0.027	0.487 ± 0.029	0.7779	−0.995	0.467 ± 0.010	0.265 ± 0.014
	−0.986	1.397 ± 0.026	0.434 ± 0.029		−0.985	0.519 ± 0.010	0.368 ± 0.017
	−0.969	1.423 ± 0.029	0.455 ± 0.029		−0.968	0.584 ± 0.012	0.419 ± 0.018
0.6693	−0.995	1.440 ± 0.021	0.498 ± 0.022	0.7858	−0.995	0.422 ± 0.009	0.249 ± 0.012
	−0.986	1.500 ± 0.021	0.574 ± 0.025		−0.985	0.453 ± 0.009	0.357 ± 0.016
	−0.969	1.518 ± 0.022	0.501 ± 0.023		−0.968	0.492 ± 0.010	0.417 ± 0.017
0.6760	−0.995	1.483 ± 0.020	0.593 ± 0.023	0.7937	−0.995	0.357 ± 0.007	0.237 ± 0.011
	−0.986	1.469 ± 0.019	0.646 ± 0.025		−0.985	0.393 ± 0.008	0.296 ± 0.013
	−0.969	1.522 ± 0.021	0.576 ± 0.024		−0.968	0.449 ± 0.009	0.371 ± 0.015
0.6828	−0.995	1.551 ± 0.017	0.604 ± 0.019	0.8017	−0.995	0.312 ± 0.007	0.209 ± 0.010
	−0.986	1.564 ± 0.016	0.652 ± 0.021		−0.985	0.357 ± 0.008	0.330 ± 0.014
	−0.969	1.565 ± 0.018	0.649 ± 0.020		−0.967	0.418 ± 0.009	0.423 ± 0.016
0.6897	−0.995	1.518 ± 0.016	0.653 ± 0.020	0.8098	−0.995	0.284 ± 0.006	0.194 ± 0.010
	−0.986	1.522 ± 0.016	0.680 ± 0.021		−0.985	0.316 ± 0.007	0.286 ± 0.013
	−0.969	1.550 ± 0.018	0.630 ± 0.020		−0.967	0.351 ± 0.008	0.394 ± 0.015
0.6967	−0.995	1.431 ± 0.016	0.640 ± 0.019	0.8179	−0.995	0.246 ± 0.006	0.164 ± 0.009
	−0.985	1.445 ± 0.016	0.670 ± 0.021		−0.985	0.301 ± 0.007	0.265 ± 0.012
	−0.969	1.476 ± 0.017	0.637 ± 0.020		−0.967	0.358 ± 0.008	0.373 ± 0.014

Table I. *(Continued)*

P_π (GeV/c)	$\cos\theta_{c.m.}$	$\pi^- p \to \pi^- p$ $d\sigma/d\Omega$ (mb/sr)	$\pi^- p \to \pi^0 n$ $d\sigma/d\Omega$ (mb/sr)	P_π (GeV/c)	$\cos\theta_{c.m.}$	$\pi^- p \to \pi^- p$ $d\sigma/d\Omega$ (mb/sr)	$\pi^- p \to \pi^0 n$ $d\sigma/d\Omega$ (mb/sr)
0.8262	−0.995	0.222 ± 0.005	0.184 ± 0.009	0.9132	−0.995	0.165 ± 0.004	0.218 ± 0.009
	−0.985	0.268 ± 0.006	0.278 ± 0.012		−0.984	0.279 ± 0.006	0.441 ± 0.014
	−0.967	0.335 ± 0.008	0.374 ± 0.014		−0.966	0.414 ± 0.008	0.596 ± 0.016
0.8345	−0.995	0.198 ± 0.005	0.158 ± 0.008	0.9224	−0.995	0.170 ± 0.005	0.218 ± 0.010
	−0.985	0.244 ± 0.006	0.268 ± 0.011		−0.984	0.303 ± 0.007	0.406 ± 0.015
	−0.967	0.319 ± 0.007	0.396 ± 0.014		−0.966	0.448 ± 0.009	0.548 ± 0.017
0.8429	−0.995	0.180 ± 0.005	0.140 ± 0.008				
	−0.985	0.244 ± 0.006	0.271 ± 0.012	0.9317	−0.995	0.197 ± 0.007	0.246 ± 0.014
	−0.967	0.326 ± 0.007	0.406 ± 0.014		−0.984	0.338 ± 0.009	0.417 ± 0.019
0.8514	−0.995	0.178 ± 0.005	0.142 ± 0.008		−0.966	0.478 ± 0.012	0.634 ± 0.024
	−0.985	0.235 ± 0.006	0.272 ± 0.012	0.9410	−0.995	0.210 ± 0.006	0.223 ± 0.011
	−0.967	0.314 ± 0.007	0.406 ± 0.014		−0.984	0.358 ± 0.008	0.383 ± 0.016
					−0.966	0.517 ± 0.011	0.629 ± 0.021
0.8599	−0.995	0.168 ± 0.004	0.142 ± 0.008	0.9505	−0.995	0.229 ± 0.006	0.265 ± 0.012
	−0.985	0.241 ± 0.005	0.291 ± 0.012		−0.984	0.375 ± 0.008	0.445 ± 0.017
	−0.967	0.329 ± 0.007	0.420 ± 0.014		−0.966	0.535 ± 0.011	0.700 ± 0.022
0.8686	−0.995	0.156 ± 0.004	0.161 ± 0.008	0.9601	−0.995	0.244 ± 0.007	0.306 ± 0.015
	−0.985	0.225 ± 0.005	0.305 ± 0.012		−0.984	0.411 ± 0.010	0.461 ± 0.020
	−0.967	0.322 ± 0.007	0.438 ± 0.014		−0.966	0.558 ± 0.013	0.736 ± 0.025
0.8773	−0.995	0.157 ± 0.004	0.171 ± 0.008				
	−0.985	0.234 ± 0.005	0.306 ± 0.012	0.9697	−0.995	0.251 ± 0.007	0.309 ± 0.014
	−0.967	0.341 ± 0.007	0.468 ± 0.015		−0.984	0.423 ± 0.009	0.505 ± 0.019
0.8862	−0.995	0.165 ± 0.004	0.183 ± 0.008		−0.966	0.550 ± 0.012	0.743 ± 0.024
	−0.984	0.244 ± 0.005	0.302 ± 0.012	0.9795	−0.995	0.251 ± 0.006	0.330 ± 0.013
	−0.967	0.366 ± 0.007	0.447 ± 0.014		−0.984	0.434 ± 0.008	0.495 ± 0.017
					−0.965	0.623 ± 0.011	0.820 ± 0.022
0.8951	−0.995	0.163 ± 0.004	0.183 ± 0.008	0.9893	−0.995	0.276 ± 0.007	0.377 ± 0.016
	−0.984	0.258 ± 0.006	0.316 ± 0.012		−0.984	0.460 ± 0.010	0.584 ± 0.022
	−0.966	0.371 ± 0.007	0.538 ± 0.016		−0.965	0.653 ± 0.014	0.830 ± 0.026
0.9041	−0.995	0.165 ± 0.004	0.200 ± 0.009	0.9993	−0.995	0.268 ± 0.009	0.380 ± 0.020
	−0.984	0.263 ± 0.006	0.353 ± 0.013		−0.984	0.459 ± 0.013	0.562 ± 0.027
	−0.966	0.393 ± 0.008	0.514 ± 0.015		−0.965	0.639 ± 0.017	0.795 ± 0.033

between the neutron-counter rings, error correlations over the different angles should be assumed small.

For the purposes of comparison, we have made a small linear extrapolation of the present data to $\cos\theta_{c.m.} = -1$, where $\theta_{c.m.}$ is the scattering angle in the c.m. system. A marked feature of the elastic-scattering cross section at 180° (Fig. 5) is the sharp change in its energy dependence between 0.6828 GeV/c and 0.6897 GeV/c, an effect of the opening of the ηN channel. There is good agreement between the measurement of Rothschild *et al.*[9] and the present data over most of the momentum range. However, there is disagreement with the cross sections of Crabb *et al.*[10] between 0.70 GeV/c and 0.85 GeV/c, much of it clearly due to a disparity between the momentum scales. An independent check of the technique used in this paper for determining the momentum scale can be obtained from the measured mass of the η and other mesons. For example, using Particle Data Group value of m_η, the cusp is predicted to occur at a momentum of 0.6855 GeV/c. Existing phase-shift solutions (not shown) do not follow the detailed behavior across the threshold. The data are inadequate for an analysis of the shape of the cusp itself to be possible.

The charge-exchange extrapolated cross sections are in good agreement with the measured 180° points of Hyman *et al.* This last experiment did not extend above 0.8 GeV/c, and at higher incident momenta there were no existing cross-section data for this reaction close to $\cos\theta_{c.m.} = -1$. However, expansions of the differential cross sections of Bulos *et al.*[11] at 0.860 GeV/c and 0.930 GeV/c had suggested that the backward cross sections dipped to very low values. It has been noted[12] that these extrapolations violate the lower isospin bound as calculated from the backward $\pi^+ p$ and $\pi^- p$ elastic cross sections of Rothschild *et al.*[9] Figure 6 shows how, far from violating these isospin bounds, the present data lie well within them. From the present data, it is calculated that, above 0.770 GeV/c, there is an unusually constant phase difference of 95 ± 5° between the $I = \frac{1}{2}$ and $I = \frac{3}{2}\pi N$ amplitudes. Existing phase-shift solutions do not

TABLE II. Differential cross sections for the reaction $\pi^- p \to \eta n$.

P_π (GeV/c)	$\cos\theta_{\text{c.m.}}$	$d\sigma/d\Omega$ (mb/sr)	$\cos\theta_{\text{c.m.}}$	$d\sigma/d\Omega$ (mb/sr)	$\cos\theta_{\text{c.m.}}$	$d\sigma/d\Omega$ (mb/sr)
0.6967	−0.937	0.097 ± 0.002	−0.804	0.091 ± 0.002	−0.537	0.067 ± 0.002
0.7037	−0.960	0.133 ± 0.004	−0.877	0.124 ± 0.004	−0.725	0.134 ± 0.004
0.7108	−0.969	0.142 ± 0.005	−0.908	0.140 ± 0.005	−0.796	0.145 ± 0.005
0.7180	−0.975	0.157 ± 0.005	−0.924	0.180 ± 0.006	−0.834	0.154 ± 0.006
0.7252	−0.978	0.188 ± 0.007	−0.935	0.193 ± 0.008	−0.858	0.180 ± 0.007
0.7325	−0.981	0.199 ± 0.008	−0.942	0.191 ± 0.008	−0.874	0.198 ± 0.009
0.7399	−0.983	0.207 ± 0.008	−0.948	0.216 ± 0.009	−0.886	0.198 ± 0.009
0.7474	−0.984	0.243 ± 0.009	−0.952	0.235 ± 0.010	−0.896	0.253 ± 0.011
0.7549	−0.985	0.251 ± 0.010	−0.955	0.218 ± 0.010	−0.903	0.235 ± 0.011
0.7625	−0.986	0.226 ± 0.009	−0.958	0.236 ± 0.010	−0.909	0.218 ± 0.010
0.7702	−0.987	0.249 ± 0.009	−0.960	0.239 ± 0.010	−0.914	0.241 ± 0.011
0.7779	−0.987	0.247 ± 0.010	−0.962	0.259 ± 0.011	−0.918	0.253 ± 0.011
0.7858	−0.988	0.240 ± 0.009	−0.964	0.235 ± 0.010	−0.922	0.226 ± 0.010
0.7937	−0.988	0.276 ± 0.009	−0.965	0.239 ± 0.010	−0.925	0.224 ± 0.010
0.8017	−0.989	0.225 ± 0.009	−0.966	0.231 ± 0.010	−0.927	0.215 ± 0.010
0.8098	−0.989	0.249 ± 0.009	−0.967	0.261 ± 0.011	−0.930	0.214 ± 0.010
0.8179	−0.989	0.229 ± 0.009	−0.968	0.254 ± 0.011	−0.932	0.226 ± 0.010
0.8262	−0.990	0.258 ± 0.009	−0.969	0.234 ± 0.010	−0.934	0.220 ± 0.010
0.8345	−0.990	0.257 ± 0.009	−0.970	0.239 ± 0.010	−0.935	0.227 ± 0.010
0.8429	−0.990	0.230 ± 0.009	−0.971	0.243 ± 0.010	−0.937	0.252 ± 0.011
0.8514	−0.990	0.263 ± 0.010	−0.971	0.227 ± 0.010	−0.938	0.203 ± 0.010
0.8599	−0.991	0.262 ± 0.010	−0.972	0.242 ± 0.010	−0.939	0.203 ± 0.010
0.8686	−0.991	0.226 ± 0.009	−0.972	0.222 ± 0.010	−0.941	0.205 ± 0.010
0.8773	−0.991	0.257 ± 0.010	−0.973	0.211 ± 0.010	−0.942	0.206 ± 0.010
0.8862	−0.991	0.265 ± 0.010	−0.973	0.268 ± 0.011	−0.943	0.213 ± 0.010
0.8951	−0.991	0.246 ± 0.010	−0.974	0.248 ± 0.011	−0.943	0.225 ± 0.010
0.9041	−0.991	0.285 ± 0.010	−0.974	0.205 ± 0.010	−0.944	0.202 ± 0.010
0.9132	−0.991	0.241 ± 0.009	−0.975	0.206 ± 0.010	−0.945	0.184 ± 0.009
0.9224	−0.992	0.267 ± 0.011	−0.975	0.228 ± 0.012	−0.946	0.199 ± 0.011
0.9317	−0.992	0.269 ± 0.015	−0.975	0.239 ± 0.016	−0.946	0.179 ± 0.014
0.9410	−0.992	0.216 ± 0.012	−0.975	0.190 ± 0.012	−0.947	0.200 ± 0.013
0.9505	−0.992	0.202 ± 0.011	−0.976	0.191 ± 0.012	−0.948	0.138 ± 0.011
0.9601	−0.992	0.163 ± 0.012	−0.976	0.198 ± 0.014	−0.948	0.134 ± 0.012
0.9697	−0.992	0.187 ± 0.012	−0.976	0.172 ± 0.013	−0.948	0.128 ± 0.011
0.9795	−0.992	0.167 ± 0.010	−0.976	0.143 ± 0.010	−0.949	0.126 ± 0.010
0.9893	−0.992	0.161 ± 0.012	−0.977	0.135 ± 0.012	−0.949	0.126 ± 0.012
0.9993	−0.992	0.156 ± 0.015	−0.977	0.179 ± 0.018	−0.950	0.089 ± 0.013

predict this behavior.

Several partial-wave analyses have studied the ηN channel, both singly and in conjunction with other reactions. A recent single-channel analysis has fitted $\pi^- p$ η production data up to $p^* = 400$ MeV/c.[13]. It can be seen from Fig. 7 that the predictions of this solution for 180° are in very poor agreement with our extrapolated cross sections in the incident momentum range 0.8 GeV/c to 0.9 GeV/c. The measurements of Hyman *et al.*[4] on the backward production of η's, which were not included in the analysis, also differ from the predictions in this range.

We have fitted the present data on η production, together with existing differential cross sections below 1.005 GeV/c,[4,11,14] with a model which includes only direct-channel poles and resonances. The following have been considered: $N(938)$, $P_{11}(1465)$, $S_{11}(1515)$, $D_{13}(1520)$, $D_{15}(1670)$, $F_{15}(1685)$, $S_{11}(1700)$, $P_{11}(1760)$. Resonances above threshold have been parametrized in the form

$$T_l^R = \frac{(x_1 x_3)^{1/2}}{\epsilon - i}, \quad \epsilon = \frac{2(E_0 - E)}{\Gamma},$$

where $x_i = \Gamma_i/\Gamma$ and $\Gamma = \Gamma_1 + \Gamma_2 + \Gamma_3$, the partial widths of the elastic, pion production, and η pro-

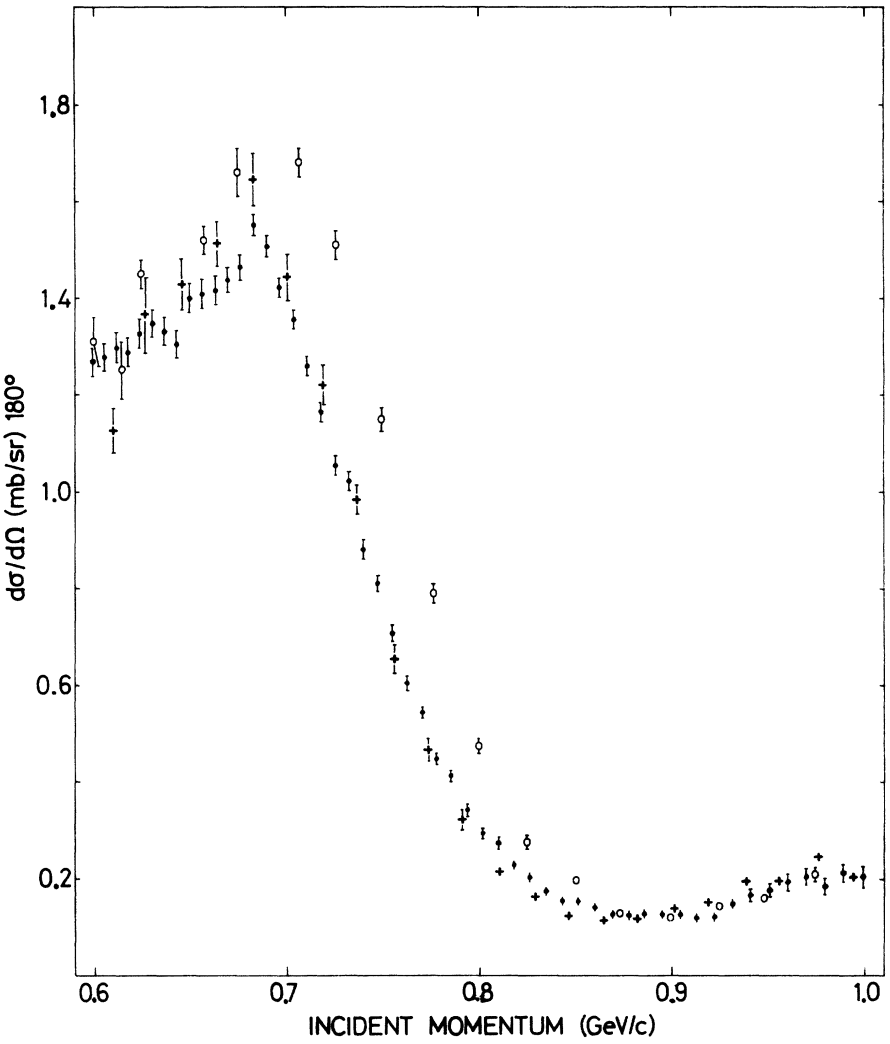

FIG. 5. Differential cross sections for $\pi^- p \to \pi^- p$ at $\cos\theta_{\text{c.m.}} = -1$. Closed circles are extrapolations of present data; crosses are the measurements of Rothschild *et al.* (Ref. 9); and open circles are the extrapolations of Crabb *et al.* (Ref. 10). The abrupt change in the cross-section behavior at the η production threshold is clearly shown, as is the large discrepancy between the data of Ref. 10 and the other two data sets on the falling edge.

duction channels. These varied with k_i, the c.m. momentum in the ith channel as

$$\Gamma_i = \gamma_i k_i B_l(k_i R) ,$$

where γ_i is constant, and B_l is the barrier-penetration factor.[15] When allowed to vary, the radius of interaction R generally preferred to assume a small value, so that the partial widths varied approximately as k_i^{2l+1}. Although the $P_{11}(1465)$ resonance mass lies below the threshold for η production, its partial width to ηN is assumed to have a similar variation. Other forms of T_l^R in which the total width Γ is restrained for energies above the resonance mass E_0 have not led to improved fits[16].

In the fits, the resonance parameters, x_1, Γ, and E_0, were constrained to lie within the ranges of values given in Table III, which ensured that they were consistent with the values determined in πN phase-shift analyses.

Small background amplitudes in the S_{11} and P_{11} waves were conveniently parametrized as if contributed by the s-channel nucleon pole. Fits were separately made for a series of masses of the lower S_{11} resonance. The values of the amplitude of this resonance, $(x_1 x_3)^{1/2}$, and χ^2/D.F. varied with the S_{11} mass as shown in Fig. 8. The findings are in general agreement with those of Ref. 16. However, our resonance amplitude assumes a somewhat higher value, which is not consistent with the predictions of SU_3.[17] If the nucleon pole was included as a zero-width resonance, $P_{11}(938)$,

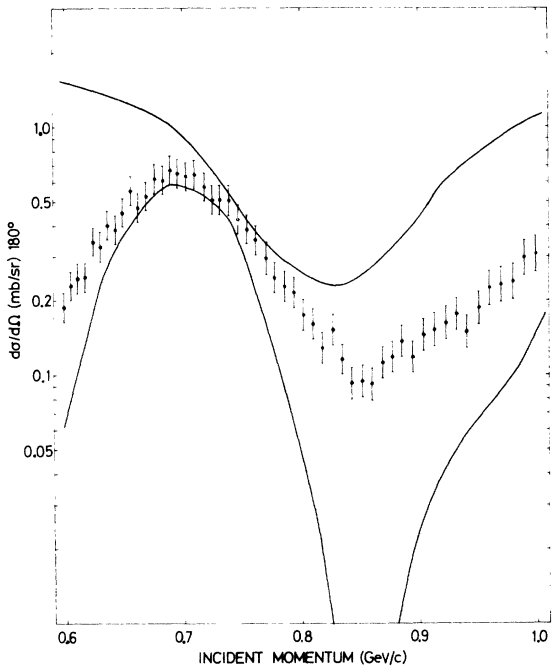

FIG. 6. Differential cross sections for $\pi^- p \to \pi^0 n$ extrapolated from the present measurements to $\cos\theta_{\text{c.m.}} = -1$. The full lines are the isospin bounds on the charge-exchange reaction calculated from the backward $\pi^+ p$ and $\pi^- p$ elastic-scattering data of Ref. 9. Experimental errors presumably mask a sharp change in the slope at the η threshold.

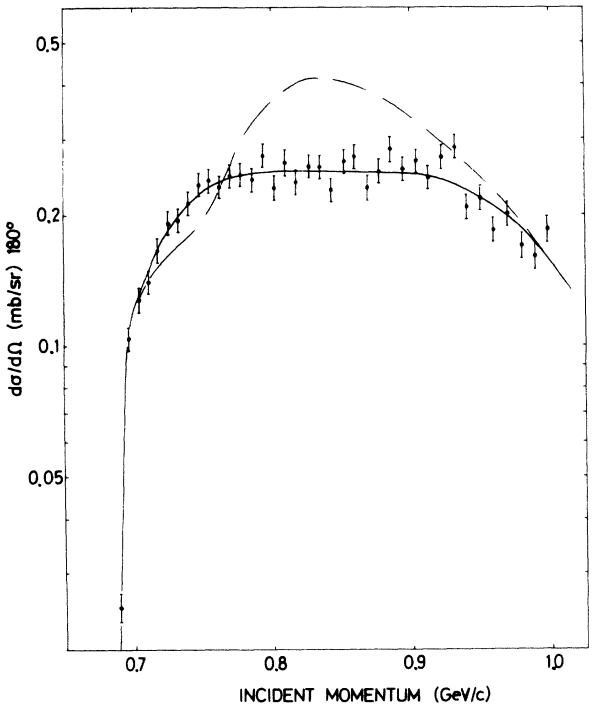

FIG. 7. Differential cross sections for $\pi^- p \to \eta n$ extrapolated from the present measurements to $\cos\theta_{\text{c.m.}} = -1$. The dashed line is the phase-shift-analysis prediction of Ref. 13; and the solid line is the result of a single-channel analysis, which fits existing data below $p^* = 400$ MeV/c with a model incorporating only direct channel-resonances and poles.

TABLE III. Resonances used in the phase-shift analysis of the ηN channel, with the limits to which their masses, E_0, total widths, Γ, and elasticities, x_1, were constrained in the fits. Also given are their fitted amplitudes at resonance, $(x_1 x_3)^{1/2}$, and the percentage changes in χ^2 per degree of freedom (D.F.) when the resonance was excluded from the fit. The effect of the inclusion of a narrow P_{11} (1530) resonance, as used in Ref. 13, is also shown. The fits have 300 degrees of freedom.

	E_0 (MeV)	Γ (MeV)	x_1	$x_1 x_3^{1/2}$	$\Delta(\chi^2/\text{D.F.})$ (%)
$P_{11}(1465)$	1460–1470	160–240	0.55–0.60		+5
$S_{11}(1515)$	1505–1545	50–100	0.25–0.35	+0.39	
$D_{13}(1520)$	1515–1525	110–130	0.50–0.58	+0.02	+37
$D_{15}(1670)$	1660–1680	125–165	0.38–0.48	−0.06	+6
$F_{15}(1685)$	1680–1690	120–140	0.58–0.62	+0.04	+3
$S_{11}(1700)$	1675–1725	100–200	0.50–0.70	−0.1	+4
$P_{11}(1760)$	1720–1800	200–400	0.20–0.40	+0.01	0
$P_{11}(1530)$	1530	65	0.12	+0.06[a]	0
$P_{11}(1530)$	1530	65	0.12	+0.23[b]	+30

[a] Amplitude of resonance fitted.
[b] Amplitude fixed at value quoted in Ref. 13.

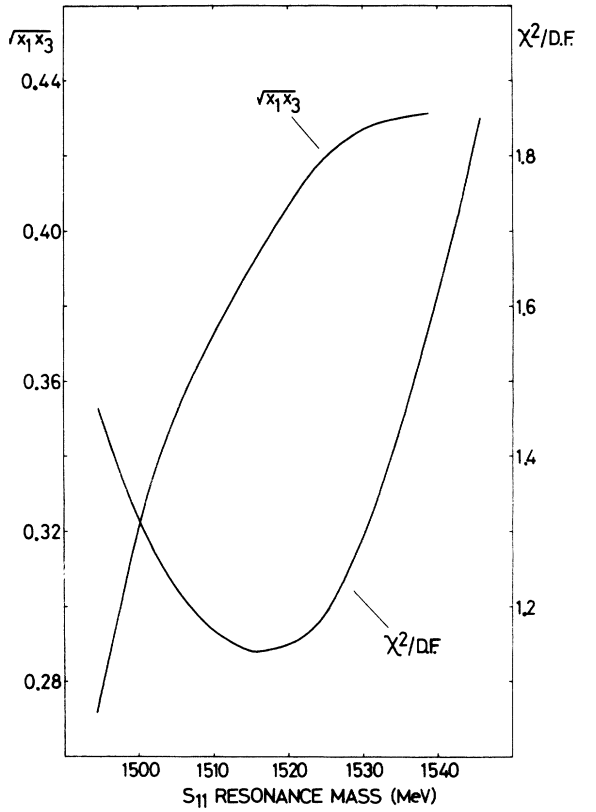

FIG. 8. The variations of the $S_{11}(1515)$ amplitude at resonance $[(x_1 x_3)^{1/2}]$ and χ^2/degree of freedom (D.F.) with the resonance mass of the S_{11}.

even higher values of the S_{11} amplitude were required, while values of χ^2 were increased by 15%. A third model, in which the u-channel nucleon pole supplemented the direct-channel pole, led to no improvement of the fits.

In agreement with Ref. 13, we find that the $D_{13}(1520)$, with a small positive amplitude of +0.02, is necessary to fit the data. The $P_{11}(1465)$ and $D_{15}(1670)$ also gave significant improvements to the fitting, while, for data below 1 GeV/c, the inclusion of the $S_{11}(1700)$, the $P_{11}(1760)$, and the $F_{15}(1685)$ was not important. We found no improvement when including a narrow P_{11} resonance of mass 1530 MeV, and a large amplitude for this resonance, such as was suggested in Ref. 13, was inconsistent with our data. In general, we find that the present data are well fitted by the direct-channel model, which, as can be seen in Fig. 7, is capable of reproducing the somewhat flattened shape of the variation of the backward cross sections with energy.

It is noteworthy, that in none of the channels is there evidence for a narrow N^* or similar such effect apart from the η cusp. C.m. energies from 1430 to 1670 MeV are continuously covered by the experiment, and are measured with a FWHM resolution ranging from 4.5 MeV to 6.6 MeV in this range. The sensitivity to such effects, which would be characterized by sudden changes with beam momentum, is limited by statistical errors only. These varied, with channel and momentum, between about 3%, and 8% at each momentum interval.

IV. SUMMARY

In conclusion, high-resolution data on the three reactions $\pi^- p \to \pi^- p$, $\pi^0 n$, and ηn close to 180° from 0.6 to 1.0 GeV/c have been presented. The data on elastic scattering generally confirm the previous measurements of Rothschild *et al.*[9] and disagree with those of Crabb *et al.*[10] The data clearly show the effect of the crossing of the ηn threshold on the $\pi^- p$ scattering channel. The charge-exchange measurements help to fill a gap in existing data near 180° and make it clear that there is no evidence for any violation of I-spin bounds in πN scattering in this region. The new data presented in η production have been included with other data on this channel below 1.005 GeV/c and have been adequately described using s-channel resonances as determined from analyses of πN scattering. Also, there is no evidence for any narrow N^* over the momentum range investigated.

ACKNOWLEDGMENTS

We wish to acknowledge the assistance of Mr. R. F. Hobbs, Mr. D. G. Miller, and Mr. D. Scholes in the construction and installation of the apparatus.

---

*Now at CERN, Geneva, Switzerland.

[1]D. M. Binnie, L. Camilleri, N. C. Debenham, A. Duane, D. A. Garbutt, J. R. Holmes, J. Keyne, M. Lewis, I. Siotis, P. N. Upadhyay, I. F. Burton, and J. G. McEwen, Phys. Rev. D 8, 2789 (1973).

[2]D. M. Binnie and A. Duane, Nucl. Instrum. Methods 77, 329 (1970).

[3]The simulation of the interactions of the decay products with the γ counters was based, where possible, on the measured performance of the detectors, or else on their predicted efficiencies. Details of this and other aspects of the Monte Carlo program are given in Ref. 1.

[4]E. Hyman, W. Lee, J. Peoples, J. Schiff, C. Schultz, and S. Stein, Phys. Rev. 165, 1437 (1968).

[5]B. C. Barish, R. J. Kurz, V. Perez-Mendez, and J. Soloman, Phys. Rev. 135, B416 (1964).

[6]N. R. Stanton, Report No. COO-1545-92, 1971 (unpub-

lished).
[7]D. G. Crabb, J. G. McEwen, E. G. Auld, and A. Langsford, Nucl. Instrum. Methods 48, 87 (1967); R. J. Kurz, Lawrence Radiation Laboratory Report No. UCRL-11339, 1964 (unpublished).
[8]Momenta and binding energies of C-12 nucleons taken from U. Amaldi, Jr., G. Campos Venuti, G. Cortellessa, C. Fronterotta, A. Reale, P. Salvadori, and P. Hillman, Phys. Rev. Lett. 13, 341 (1964); U. Amaldi, Jr., G. Campos Venuti, G. Cortellessa, E. de Sanctis, S. Frullani, R. Lombard, and P. Salvadori, Phys. Lett. 25B, 24 (1967).
[9]R. E. Rothschild, T. Bowen, P. K. Caldwell, D. Davidson, E. W. Jenkins, R. M. Kalbach, D. V. Petersen, and A. E. Pifer, Phys. Rev. D 5, 499 (1972).
[10]D. G. Crabb, R. Keller, J. R. O'Fallon, T. J. Richards, R. J. Ott, J. Va'ura, and L. S. Schroeder, Phys. Rev. Lett. 27, 216 (1971).
[11]F. Bulos *et al.* (Brandeis-Brown-Harvard-MIT-Padova Collaboration), Phys. Rev. 187, 1827 (1969).
[12]N. A. Tornqvist, Phys. Lett. 40B, 109 (1972), and references therein.
[13]Y. Lemoigne, P. Ganet, P. Marty, R. Ayed, P. Bareyre, P. Borgeaud, M. David, J. Ernwein, J. Feltesse, and G. Villet, in *Baryon Resonances–73,* edited by E. C. Fowler (Purdue University, West Lafayette, Indiana, 1973).
[14]W. B. Richards, C. B. Chiu, R. D. Eandi, A. C. Helmholz, R. W. Kenney, B. J. Moyer, J. A. Poirier, R. J. Cence, V. Z. Peterson, N. K. Schgal, and V. J. Stenger, Phys. Rev. D 1, 10 (1970); W. Deinet, H. Muller, D. Schmitt, H. M. Standenmaier, S. Buniatov, and E. Zavattini, Nucl. Phys. B11, 495 (1969).
[15]J. M. Blatt and V. F. Weisskopf, *Theoretical Nuclear Physics* (Wiley, New York, 1956).
[16]S. R. Deans and J. E. Rush, Particles and Nuclei 2, 349 (1971).
[17]N. P. Samios, M. Goldberg, and B. T. Meadows, Rev. Mod. Phys. 46, 49 (1974).